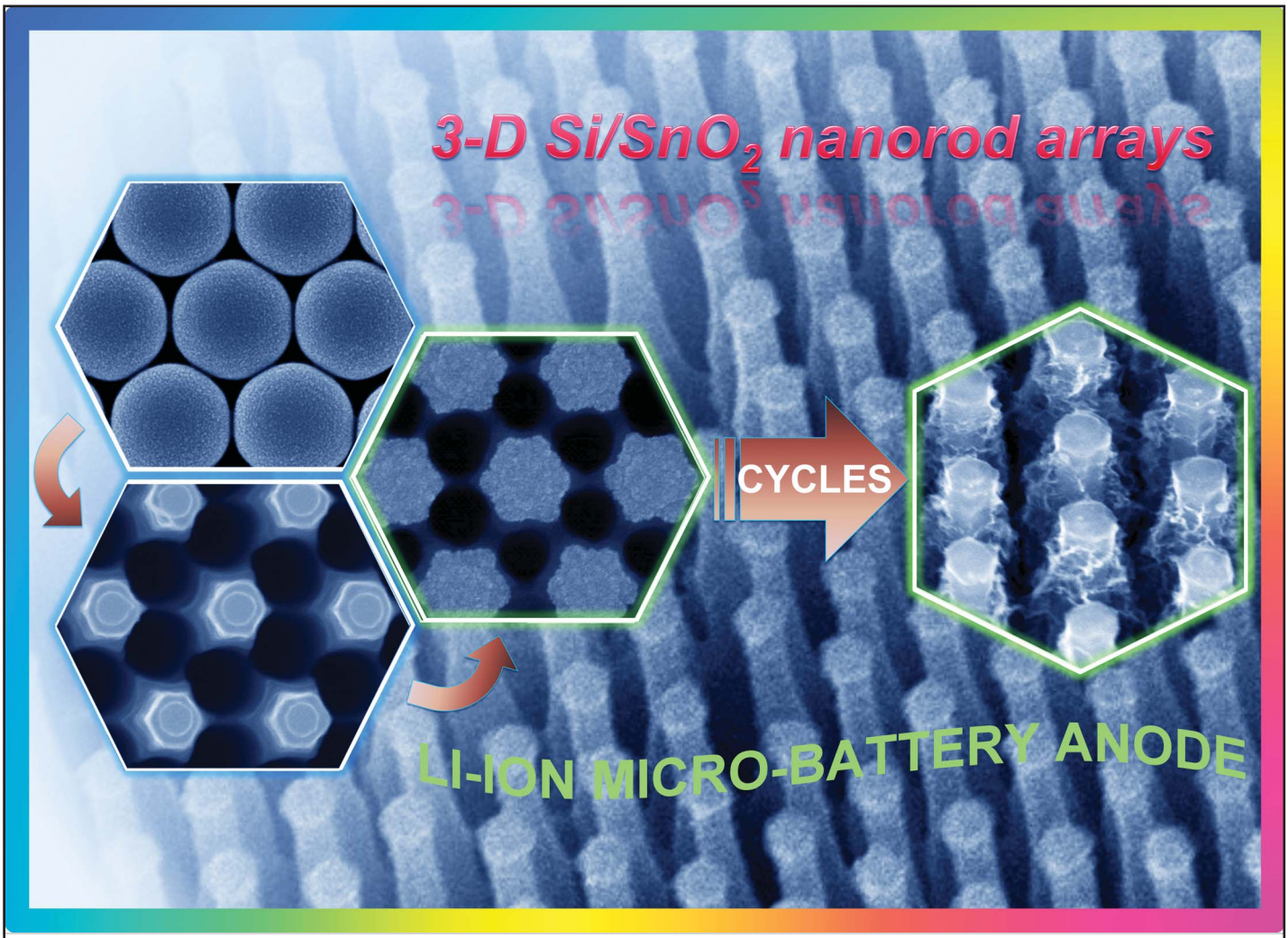

A wafer scale fabrication of 3D Si based nanocomposite arrays as anodes for on chip micro-LIBs has been performed in the Mircoenergy Group of A/P Dr. Jing Li and Prof. Junyong Kang at Xiamen University.

Title: Fabrication of 3D hexagonal bottle-like Si–SnO_2 core–shell nanorod arrays as anode material in on chip micro-lithium-ion-batteries

This work introduces the fabrication of 3D Si–SnO_2 arrays as anode in micro-LIBs with the volume expansion and electrochemical kinetic issues addressed, which will facilitate the configuration of solid state micro-batteries for power supply in micro-electronic devices.

As featured in:

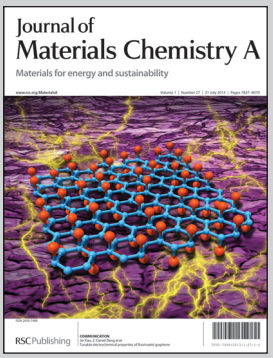

See C. Yue *et al.*,
J. Mater. Chem. A, 2013, **1**, 7896.

RSC Publishing

www.rsc.org/MaterialsA

Registered Charity Number 207890

Journal of Materials Chemistry A

RSC Publishing

PAPER

View Article Online
View Journal | View Issue

Cite this: J. Mater. Chem. A, 2013, 1, 7896

Fabrication of 3D hexagonal bottle-like Si–SnO_2 core–shell nanorod arrays as anode material in on chip micro-lithium-ion-batteries†

Chuang Yue,[a] Yingjian Yu,[a] Jun Yin,[ab] Tailun Wong,[c] Yashu Zang,[a] Jing Li*[a] and Junyong Kang[a]

Received 7th February 2013
Accepted 24th April 2013

DOI: 10.1039/c3ta10601b

www.rsc.org/MaterialsA

Three-dimensional (3D) Si–SnO_2 composite core–shell nanorod arrays were fabricated as the anode material in lithium ion micro-batteries by nanosphere lithography (NSL) combined with inductive coupled plasma (ICP) dry etching technology. The hexagonal bottle-like Si NR arrays in wafer scale with homogeneous morphology and good mechanical structure provide enough space to accommodate the volume expansion during Li ion insertion/de-insertion processes, while the additionally deposited SnO_2 thin film was prepared to successfully improve the capacities and cycle performance by configuring the 3D Si–SnO_2 NR composite electrode arrays. This fabrication method has the advantages of simplicity, large scale production, easy size and shape manipulations, low cost and Si-process compatibility. This work will facilitate the configuration of solid state micro-batteries for power supply in micro-electronic devices, such as MEMS devices or smart IC chips.

Introduction

In recent years, as the integrated circuit (IC) technologies and Micro/Nano-Electro-Mechanical System (M/NEMS) develop rapidly, more and more micro/nano devices are fabricated or commercialized.[1–3] But the lagged pace of battery miniaturization hinders the further scaling down or long lasting life of those devices. Moreover, it becomes inconceivable to integrate the power supply system within the device structure when reducing the sizes of all kinds of micro devices into the nano scale. Among various energy storage systems, the rechargeable lithium ion battery (LIB) is a predominant power source due to its relatively high energy density and long life time.[4–6] Traditional thin film rechargeable LIBs designed in two dimensional (2D) geometries need large footprint areas to achieve large capacities, resulting in a compromise between the energy and power densities.[7,8] Therefore, many researchers have begun to turn towards 3D rechargeable LIBs with higher power and energy densities in a small footprint area.[9,10] Various 3D Li-battery structures have been configured based on 3D current collectors,[11,12] electrodes,[13,14] or electrolytes.[15] Additionally, a 3D-integrated all-solid-state battery has been successfully fabricated using thin film amorphous silicon as the anode material by the low pressure chemical vapor deposition (LPCVD) technique.[16,17]

Silicon is the material with the most potential in the application of rechargeable micro-LIB systems, given its wide use in the semiconductor industry. It is well known that silicon has a low discharge potential of less than 0.5 V *vs.* Li/Li^+ and a high theoretical charge capacity of 4200 mA h g^{-1} with 4.2 lithium per silicon,[18] which is ten times more than that of the existing graphite anodes (372 mA h g^{-1}). However, silicon as anodes has few practical applications due to its volume expansion by 400% upon the insertion and extraction of lithium, which results in the pulverization and capacity fading of the batteries.[19] It is well accepted that fabrications of nanostructures or composite configurations are effective methods to address the volume expansion as well as electrochemical kinetic issues during Li insertion/de-insertion processes.[20–23] To date, various Si nanostructures have been synthesized, such as Si nanowires (NWs) by a supercritical fluid liquid solid (SFLS) growth technique,[20] Si nanowalls by an oblique angle deposition (OAD) technique,[21] double-walled Si/Ge composite nanotubes by a templating method[22] or C&Si nanocomposites by using a chemical vapor deposition (CVD) method,[23] and so on. All these approaches are purposed to enhance the cycle life and energy density of LIBs by providing larger buffer spaces and surface areas. Among them, Si NWs, which are chemically and electrically bonded to the current collectors, can effectively circumvent the pulverization problem.[24] However, besides the high processing cost, the employment of the metal current collectors, which are the precursors for the growth of Si NWs, and the random structures

[a]Department of Physics/Pen-Tung Sah Institute of Micro-Nano Science and Technology, Xiamen University, Xiamen, Fujian, 361005, China. E-mail: lijing@xmu.edu.cn
[b]Wuhan National Laboratory for Optoelectronics, School of Optical and Electronic Information, Huazhong University of Science and Technology, Wuhan, 430074, China
[c]Center of Super-Diamond and Advanced Films (COSDAF) and Department of Physics and Materials Science, City University of Hong Kong, Hong Kong SAR, China

† Electronic supplementary information (ESI) available. See DOI: 10.1039/c3ta10601b

of the Si NWs are not compatible with the standard silicon processing, leading to limited applications of Si NWs in most electronic devices. Recently, inductive coupled plasma (ICP) etching technology has been developed to fabricate vertically standing Si NRs as the anode materials for LIBs.[25,26] But, Si NRs with a similar average size from top to bottom for each single nanorod could experience mechanical breaking and be peeled off from the Si surface during the fabrication or charge/discharge processes, which is not favorable for power supply in the long life time required for electronic devices.

In this work, periodic 3D hexagonal Si NR arrays over a large area were fabricated using the modified nanosphere lithography (NSL) method combined with the ICP dry etching technology. As one of the most promising anode materials in LIBs and given its high theoretical capacity (781 mA h g^{-1}) and low potential of lithium ion intercalation,[27] SnO_2 was chosen to composite with Si NRs to enable improvements of electrochemical properties by solving structural stability and surface conductivity problems. 3D hexagonal Si–SnO_2 core–shell nanocomposites in a "bottle" shape with superior homogeneity and verticality were fabricated by choosing a suitable polystyrene (PS) template and optimizing the ICP etching time and cycles. The performance and mechanism during the lithium ion insertion/de-insertion in the Si–SnO_2 NR arrays were studied. The results indicate that the 3D Si–SnO_2 composite anode in nanorod arrays exhibits significantly improved mechanical stability and cycleability compared to Si NRs or planar Si. The successful fabrication of the 3D Si–SnO_2 NR arrays on Si substrates and their practical application in LIBs offer a feasible option to integrate a micro-power source into the IC systems, M/NEMS or other electronic devices.

Experimental section

The fabrication processes for Si NRs and Si–SnO_2 NR arrays are schematically shown in Scheme 1.

1 The preparation of PS nanosphere templates

A self-assembled PS nanosphere monolayer over a large area (as shown in Fig. S1(a) of ESI†) was used as a mask to produce Si NRs by ICP etching on a silicon substrate. After standard cleaning and surface activation, a PS nanosphere suspension (diameter of ~300 nm) with a concentration of 5% (wt) was spin-coated on the hydrophilic n-type Si (100) substrates (with a thickness of 280–320 μm, purchased from Shanghai Guang Wei Electronic Materials Co., Ltd.) using a commercial spin coater by modifying our previous procedures.[28] The spin-coating process consists of two steps: (i) lower speed rotation at 500 rpm for 10 s to spread the bead solution evenly; (ii) higher speed rotation at 2500 rpm for 1 min to spin away the excess PS nanosphere solution. Afterwards, O_2 plasma etching was introduced to tailor the size of the PS nanospheres by adjusting the etching time to 0, 30, and 60 s, as shown in Fig. 1, row A.

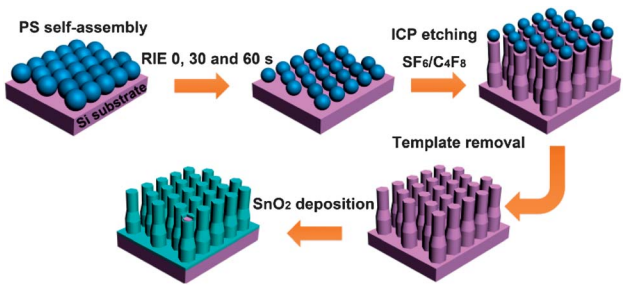

Scheme 1 Illustration of the fabrication processes for Si NRs and Si–SnO_2 NR arrays.

2 Preparation of Si NRs and Si–SnO_2 NR arrays

Hexagonal Si NRs were fabricated by etching the silicon substrates coated with the PS nanosphere template in an Alcatel-AMS 200 ICP system. During the ICP etching, SF_6 gas was applied to etch the exposed area of the Si substrate, while C_4F_8 gas was used to deposit fluorinated polymer to protect the lateral wall of the Si NR structures. These chemical species were generated using an RF power of 1000 W at a pressure of 6 mTorr. The temperature of the substrate was kept at 20 °C by cooling with a stream of helium. Alternating cycles of etching in a flow of SF_6 and passivation in a flow of C_4F_8 were performed with the total process lasting for 8 minutes. Compared to previous work,[25] the etching process was modified so that bottle-like Si NRs instead of straight NRs were produced as seen in Fig. 2.

After the ICP etching process, the PS nanospheres were removed by ultrasonic cleaning in tetrahydrofuran, acetone and alcohol for 10 minutes respectively. Then the prepared silicon substrates were cleaned by immersing in piranha solution (4 : 1 98% H_2SO_4 : 30% H_2O_2) at 80 °C for 10 min followed by dip-etching in HF (2%) to remove byproducts, a thorough rinsing with DI water and drying in a stream of nitrogen gas. Eventually, Si NRs were formed on the substrates with superior homogeneity and verticality as shown in Fig. 2. In order to fabricate Si–SnO_2 composites, an additional SnO_2 film was deposited on the Si NR arrays by radio frequency (RF) magnetron sputtering (JC-500-3/D) using a Sn target with a purity of 99.99%. During the sputtering process, the chamber pressure was kept at about 1 Pa with an Ar : O_2 ratio of 1 : 2 and the substrate was rotated to perform uniform deposition.

3 Characterization

The morphologies and structure properties of the Si NRs and Si–SnO_2 NR arrays were investigated using a Hitachi S-4800 field-emission scanning electron microscope (SEM) and JEM-2100 high resolution transmission electron microscope (HRTEM) equipped with an energy dispersive X-ray (EDX) spectrum analyzer. The crystal structures of the as-fabricated samples were characterized by PANalytical X'pert PRO X-ray diffraction (XRD) with Cu-Ka radiation (λ = 1.5406 Å) in a 2θ range of 20–72°. For the electrochemical characterization, coin cells were configured in an Ar-filled glove box with an oxygen and water level less than 1 ppm. Small pieces in the size of 10 × 10 mm^2 were cut from above fabricated samples and used as the anode material for a half-cell test. Firstly, Cr/Au with a thickness of

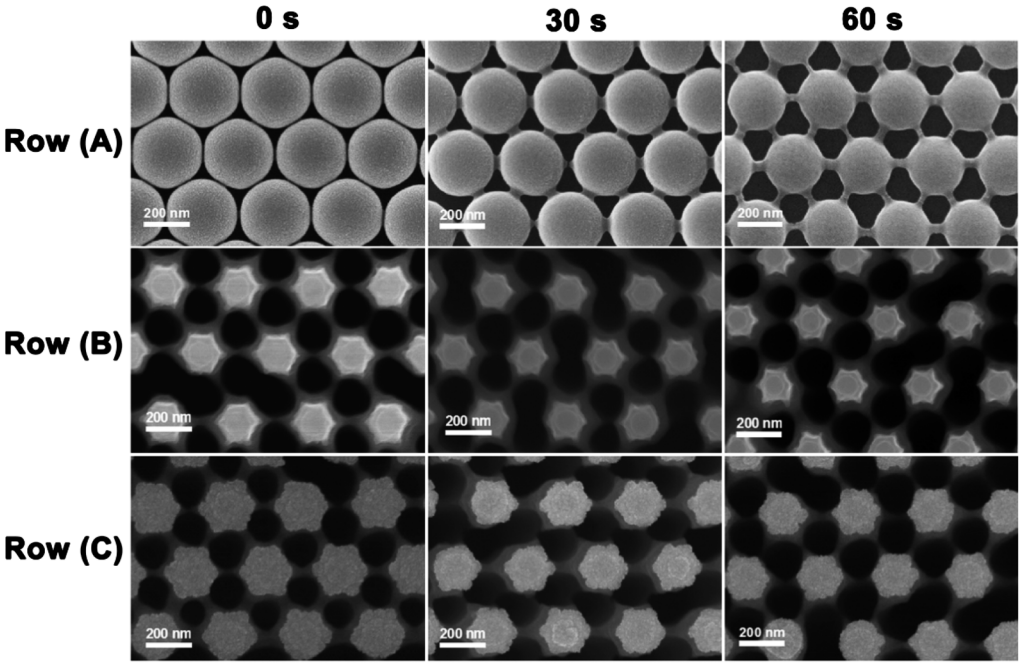

Fig. 1 Top-view SEM images of row (A) as-fabricated PS nanosphere templates with sizes adjusted by different O_2 plasma etching time of 0, 30 and 60 s, and row (B) Si NR arrays and row (c) Si–SnO_x arrays with different sizes fabricated by using the corresponding PS nanosphere templates in row (A).

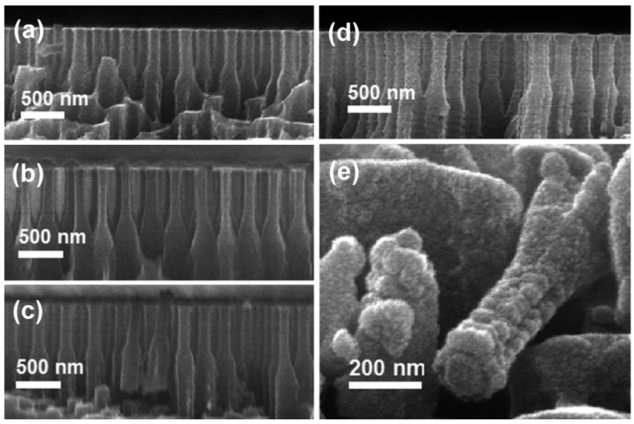

Fig. 2 Section-view SEM images of Si NRs fabricated by using the PS templates after O_2 plasma etching for (a) 0 s; (b) 30 s and (c) 60 s, respectively; (d) Si–SnO_x NRs deposited on the structure of (a); and (e) an individual Si–SnO_x NR composite in high magnification.

20/200 nm were consecutively sputtered on the back sides of the samples as the current collectors. Then coin cells (2025) were assembled using the prepared Si NRs or Si–SnO_2 NRs pieces as the electrodes, lithium metal foils as the counter electrodes, a polypropylene (PP) micro-porous film (Cellgard 2400) as the separator, and 1 M $LiPF_6$ (lithium hexafluorophosphate) in ethylene carbonate (EC) diethyl carbonate (DEC) (1 : 1 in volume) and 2% vinylene carbonate (VC) as the electrolyte. As comparisons, the cells using planar Si and Si–SnO_2 substrates, which were fabricated in the same conditions with the above samples, were also prepared. Finally, the cells were aged for 12 h before measurements. Cyclic voltammetry (CV) measurements were performed on a CHI660D electrochemical workstation (Chenhua, Shanghai) using a voltage window of 0.01–2.0 V *vs.* Li/Li^+ at a scan rate of 0.5 mV s^{-1}. The galvanostatic charge and discharge tests were conducted on a Land battery program-control test system within the voltage window from 0.13 to 2.0 V *vs.* Li/Li^+. All tests are operated at room temperature. After electrochemical measurements, the cells were disassembled and the postmortem morphologies of the active material were then imaged by SEM.

Results and discussion

1 Morphology and structural properties

Fig. 1 row (A) shows the SEM images of the as-prepared two dimensional hexagonally arranged PS nanosphere templates in monolayer dispersion on silicon substrates. The diameters of the PS nanospheres on the templates were manipulated by adjusting the O_2 plasma etching time to 0, 30 and 60 s. The different arrangements indicate that the spacing between the PS nanospheres is gradually enlarged along with the increment of the etching time. The average diameters of PS nanospheres are about 300, 270 and 240 nm after the O_2 plasma etching for 0, 30 and 60 s, respectively. This shows a linear relationship between the diameters of PS nanospheres and the RIE etching time as illustrated in Fig. S2 (ESI†), and the corresponding etching rate is about 1 nm s^{-1}. These PS templates were successfully used to manipulate the size and interspacing of the subsequently fabricated Si NR arrays by the ICP etching process. The wafer scale hexagonal Si NRs obtained by removing the above PS nanosphere templates are shown in Fig. 1 row (B) and S1(b) (ESI†). The size of the produced Si NRs is gradually reduced with

the same trend as the size changing of PS nanosphere templates in row (A). It can be easily understood that the hexagonal morphologies of Si NRs were produced by using PS nanosphere templates in monolayer dispersion with the hexagonal close packed arrangement. Additionally, in order to prepare Si–SnO_x composites, a uniform layer was sputtered on the Si NRs by using a Sn target and reaction gas of oxygen, as shown in Fig. 1 row (C). The average parallel sizes in the top surface of the hexagonal Si NRs range from 145, 135 to 125 nm and the corresponding sizes of the Si–SnO_x composites change from 205, 185 to 165 nm by using the different PS nanosphere templates.

The layouts of these three kinds of Si NRs are visualized in the section-view SEM images of Fig. 2(a)–(c) showing a periodic arrangement in the bottle-like NR morphologies except for the difference in diameters, which is consistent with the results in the top view images. The height of these Si NRs is about 1.2 μm and the upper part so called "bottleneck" is nearly 500 nm. The Si NRs are anchored firmly to the substrate and this unique structure is beneficial for the application in 3D nanostructured electrodes for microbatteries, which often experience fracture or breaking when using vertically straight NRs. After depositing SnO_x film, Si NRs with the homogeneous coverage were produced as shown in Fig. 2(d). Apparently, the NRs become larger in size with SnO_x deposition, but their shape does not change much compared with the original Si NRs and still has a bottle-like appearance. The view of an individual Si–SnO_x NR in a high magnification as seen in Fig. 2(e) further proves the hexagonal structure of the new composite NRs with a uniform deposition of the SnO_x grains in a thickness of ~20 nm. The presence of oxygen and tin content in the further EDS characterization evidences the successful deposition of SnO_x as illustrated in Fig. 3. It is obvious to see that the SnO_x films are hexagonally conformal with the Si NRs over a large area. So, the modified NSL combined dry etching process is technically feasible to fabricate the 3D hexagonal Si–SnO_x core–shell bottle-like NR arrays.

The crystal structures of the as-prepared Si NRs and Si–SnO_x composites were examined by XRD as displayed in Fig. 4. The black line represents the diffraction pattern of the Si NRs showing a distinguishable diffraction peak at 69.8° (2theta), which can be assigned to the Si (100) plane diffraction according to the reference diffraction pattern from Si JCPDS card no. 27-1402. It is well understood that the prepared Si NRs have a good crystal quality since single crystal Si (100) substrates were used in the fabrication process. Compared to the Si NRs, the diffraction pattern of the Si–SnO_x core–shell nanostructure, represented by the red line, shows resolved diffraction peaks at 26.5°, 33.9°, 51.8°and 65.0°, which correspond to the diffractions of SnO_2 (110), (101), (211) and (112) planes (JCPDS card no. 41-1445), respectively. This shows that the SnO_2 films were homogeneously deposited on those Si NR arrays with a crystalline property.

More detailed information on the morphologies and crystal structures of the Si NRs and Si–SnO_2 composites can be obtained from the TEM images, as shown in Fig. 5. Fig. 5(a) shows the part of a bottle-like Si NR, which displays a scallop-shaped sidewall produced by the periodic etching and protection during the ICP process, but with good verticality of the whole length. The ordered atom-by-atom arrangement in the high magnification as seen in Fig. 5(b) indicates the high crystal quality of the Si NRs apart from an amorphous-like layer with a thickness of less than 2 nm, which is due to surface damage caused by the plasma etching treatment. The shell of SnO_2 layer, consisting of numerous SnO_2 nano grains with sizes ranging from 5 to 10 nm, is shown in the Fig. 5(c). The whole Si NR is covered uniformly by a SnO_2 film and the original scallop-shaped edge in Si NR is almost invisible. In the HRTEM image of an individual SnO_2 shell area, as displayed in Fig. 5(d), the interplanar lattice spacing is measured to be around 0.33 nm, which corresponds to the (110) plane of SnO_2 exhibiting good consistency with the previous XRD results.

2 Electrochemical properties

Fig. 6(a) and (b) show the electrochemical responses of the Si NRs and Si–SnO_2 NR composites investigated by CV measurement at a scan rate of 0.5 mV s^{-1}. Electrochemical properties of

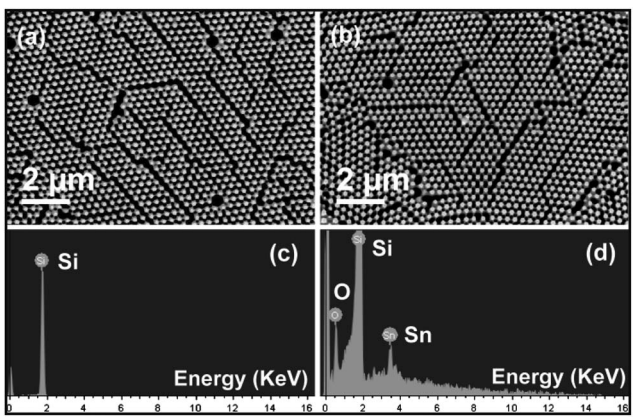

Fig. 3 Top view SEM images of (a) Si NRs and (b) Si–SnO_x NRs over a large area prepared on PS sphere templates; and the corresponding EDS patterns of (c) from the sample (a) and (d) from the sample (b).

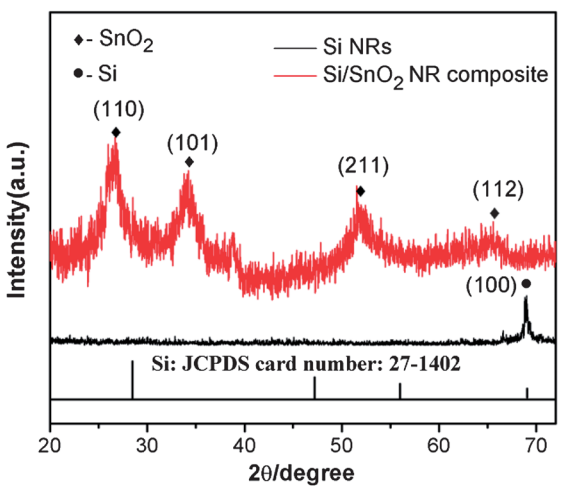

Fig. 4 XRD patterns of the Si NRs and the corresponding Si–SnO_2 NR composite.

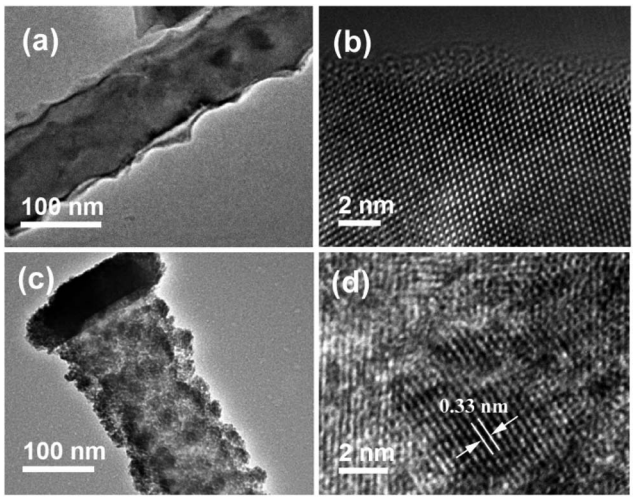

Fig. 5 TEM characterizations of the as-fabricated Si NRs and Si–SnO_2 NR composite: (a) TEM image of a single Si NR; (b) HRTEM image from the edge of the Si NR in (a); (c) TEM image of SnO_2 nano grains on the surface of a Si NR; (d) HRTEM image of a typical SnO_2 nano grain randomly taken from (c).

planar Si and planar Si–SnO_2 as anodes were also characterized for comparison as shown in Fig. 6(c) and (d). These current–potential characteristics are similar to previous experiments on microstructured Si anodes.[24,29–31] As shown in the CV curves of Si NR electrode in Fig. 6(a), during the charging process a reduction peak appears at a potential of about 300 mV *vs.* Li/Li^+ and then extends to about 100 mV at a quite large current, which is generally associated with the insertion of lithium ion into the Si active material to form Li_xSi alloys. Additionally, a reduction peak at about 80–150 mV is nearly resolved in the first several cycles and gradually decreases in the following cycles, which is suggested to be caused by the transition from Li insertion into single Si crystal to insertion into amorphous Si phase. This is consistent with the previous TEM result that a thin layer of amorphous Si was formed on the surface of each individual Si NR by the ICP etching. During the discharging process, a double peak response located at about 370 mV and 550 mV is resolved, which usually can be attributed to a Li ion partial extraction from Li_xSi alloy and a full Li-discharge resulting in amorphous Si, respectively.[29] As shown in Fig. 6(c), the CV curves in the planar Si electrode show a similar profile as that in Si NRs except for the more significant reduction peak at about 130–150 mV, which evidences the amorphous effect on the surface of Si NRs.

When depositing a thin film on the Si NR arrays, the Si–SnO_2 nanocomposite performs slightly different from Si NRs during cycling. Generally, the additional SnO_2 is involved in the electrochemical reactions as follows:

$$SnO_2 + 4Li^+ + 4e^- \rightarrow Sn + 2Li_2O \quad (1)$$

$$Sn + xLi^+ + xe^- \leftrightarrow Li_xSn \quad (2)$$

As shown in Fig. 6(b), a cathodic peak appears at around 1.0 V in the first cycle but is absent in the rest of the cycles, which can be attributed to the above irreversible reaction (1) as well as

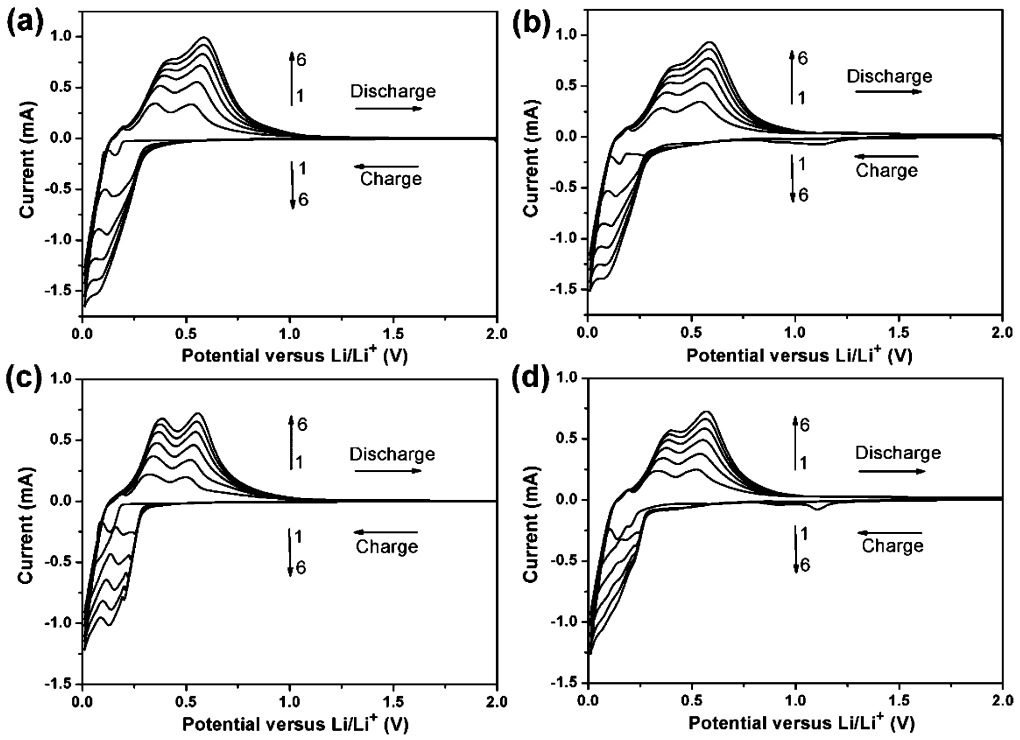

Fig. 6 Cyclic voltammogram curves of (a) Si NRs, (b) Si–SnO_2 NRs, (c) planar Si, and (d) planar Si–SnO_2 electrodes in the first six cycles within the potential window between 2.0 V and 0.01 V *versus* Li/Li^+ at a 0.5 mV s^{-1} scan rate.

the formation of a solid state electrolyte interface (SEI) film due to the deformation of electrolyte.[32,33] This phenomena also can be found in the planar Si–SnO_2 electrode, as shown in Fig. 6(d). It is worth noting that the redox peaks in all samples experience a slight movement as the cycles go on because of amorphization effects. Also, the magnitude of the current peaks increases with cycling, which is caused by the activation of more material to react with Li in each cycle.[29] However, the difference between separate cycles is gradually reduced revealing the gradual reaction saturation.

The performances of the Si NRs and Si–SnO_2 NR composite were also tested by galvanostatic discharge and charge measurements with comparison to those in planar Si and planar Si–SnO_2. In this work, during the electrochemical measurement process, it was found that when the cut-off voltage is set below 0.1 V the whole discharging (Li-ion insertion) process would hold a long working time which may be due to more and more Li ions inserting into the abundant Si substrate bulk material, which understandably would experience mechanical fractures resulting in the capacity fading and the destroying or collapse of Si NRs on it. So, in order to avoid a long discharge time and the influence of the Si substrate, a narrower voltage window of 0.1 V to 2.0 V *vs.* Li/Li^+ was employed to achieve a compromise between the capacity and the cyclability. The first and second discharge and charge voltage profiles of Si NRs and Si–SnO_2 NR composite arrays under a current density of 20 μA cm^{-2} are shown in Fig. 7(a) and (b), respectively. The plateaus at ~250 and ~125 mV during the discharge process and the plateaus at ~300 and ~500 mV during the charge process are characterized, which are consistent with the charge (Li-ion insertion) and discharge (Li-ion extraction) behaviors in the above CV results. An irreversible capacity loss during the first cycle is presented in both samples, which is generally due to the formation of an SEI layer that partly consumes the Li^+ or the irreversible reactions during Li insertion. Although the restricted Coulombic efficiencies (CE, defined as the charge capacity divided by the discharge capacity) of both Si NRs and Si–SnO_2 in the first cycle are obtained with amounts of around 42% and 56% respectively, the Si–SnO_2 NR arrays still show a higher efficiency. After the first cycle, the CEs of the two samples are improved, which is because the side reactions would cease or slow down. Moreover, the Si–SnO_2 NR arrays exhibit a better performance than that in the Si NR electrode by presenting almost two times higher capacities during the first (185 *vs.* 100 μA h cm^{-2}) and second (120 *vs.* 50 μA h cm^{-2}) cycles.

Fig. 7(c) lays out the area capacities with cycling in anode materials of the Si NRs and Si–SnO_2 NR composite as well as those in planar Si and planar Si–SnO_2 electrodes. Among them, Si–SnO_2 NR composite as an anode material shows the absolutely highest capacity and even after 40 cycles a high capacity of 0.24 mA h cm^{-2} per footprint area still can be maintained at a current density of 20 μA cm^{-2} and within a potential window of 0.13 V to 2.0 V *vs.* Li/Li^+. Interestingly, after an obvious drop in the first cycle commonly caused by some irreversible reactions, the capacity of the Si–SnO_2 NR array anode is increased in the

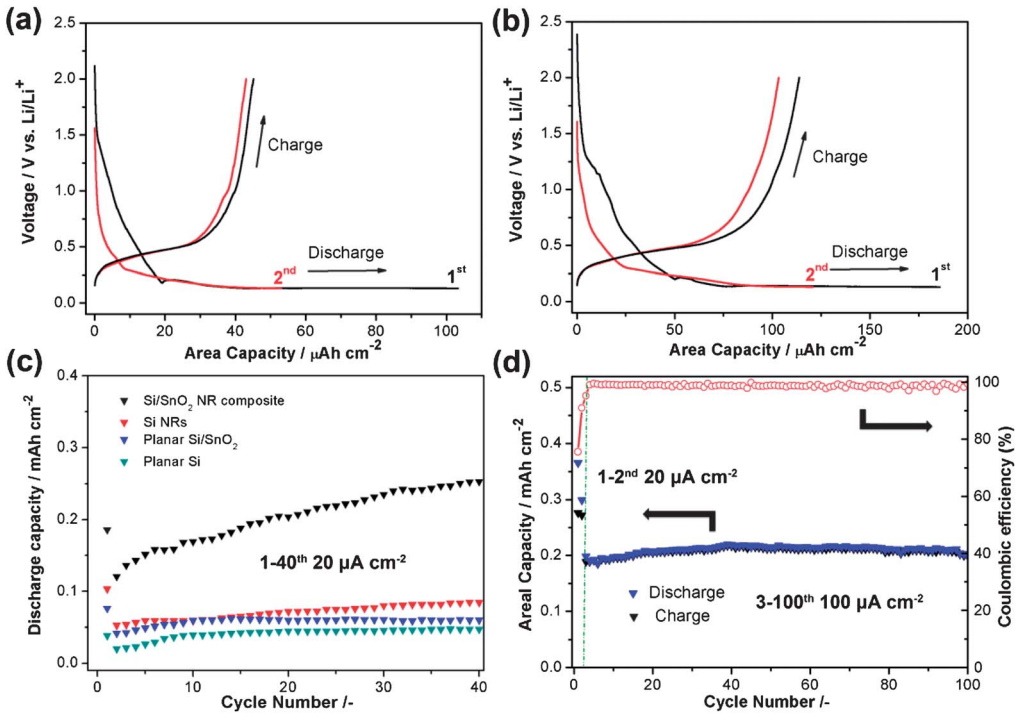

Fig. 7 Voltage profiles for (a) Si NRs and (b) Si–SnO_2 NR composite electrodes during the 1st and the 2nd cycles under a current density of 20 μA cm^{-2}; (c) the cycle performances of Si NRs and Si–SnO_2 NR composite electrodes with comparisons to those in planar Si and planar Si–SnO_2 anodes under a current density of 20 μA cm^{-2} within the voltage window from 0.13 to 2.0 V *vs.* Li/Li^+; (d) the capacity retention of the Si–SnO_2 NR composite electrode at a current density of 100 μA cm^{-2} within the voltage window between 0.1 and 2.0 V *vs.* Li/Li^+.

following several cycles, which is suggested to be due to the improved Li-ion diffusion kinetics by an activation and stabilization process during cycling and then reaching a saturation value.[34–37] In addition, compared to the planar Si substrate electrode, the Si NR electrode shows much better cyclability especially with increasing cycles. Apparently, the unique 3D nanostructure is responsible for the improved cycle performance by having a larger surface area to reduce the polarization effect and provide enough space to release stress during the Li ion insertion/extraction process.[38] On the other hand, the coating layer of the SnO_2 thin film could prevent the direct contact between the Si active material and the electrolyte, thus retarding the gradual growth of the SEI layer. Moreover, as shown in reaction (1), not only can the reduction product Sn particles act as the reversible active material (as shown in reaction (2)) by reacting with Li^+ to increase the capacity, but also the formation of the non-conducting Li_2O matrix on the Si NR surface would help to improve the performance by alleviating the volume expansion for both Si and Sn active materials during cycling.[39,40] Thus, the cycle performance can be improved by tailoring electrode configuration with an additional composite layer on the surface of the Si NRs.

As illustrated in Fig. 7(d), a larger voltage window from 0.1 to 2.0 V *vs.* Li/Li^+ can properly improve the capacity of the Si–SnO_2 NR electrode to 0.36 mA h cm^{-2} per footprint area during the first two cycles at the same charge/discharge current density of 20 μA cm^{-2}, which can be used to activate the Si NRs. While when the current density increased to 100 μA cm^{-2} in the following cycles, the capacity of the Si–SnO_2 NR arrays drops to about 0.2 mA h cm^{-2} in the third cycle but then maintains at the same level even after 100 cycles. After the activation during first two charge/discharge processes, the CE keeps as high as almost 100% until the 100th cycle. Another higher current density of 500 μA cm^{-2} charge/discharge test was also conducted to evidence the activation process and the good capacity retention in the Si–SnO_2 NR composite electrode as shown in Fig. S3 (ESI†). The sample has been activated in a CV measurement process in which higher current densities even up to 1.5 mA cm^{-2} at the peak current were imposed, which generally would cause more damage in the active materials including both the SnO_2 and Si. That's also the reason for the dramatic drop of the capacity during the first 20 cycles. But after that the capacity is well maintained at about 0.25 mA h cm^{-2} even at the high current density of 500 μA cm^{-2}. This value is quite promising with comparison to the 0.08 mA h cm^{-2} in the commercialized 2D thin film micro-LIBs.[41] Of course, there is still much space for improving the capacity of 3D micro-LIBs by using other composite materials, such as Ge or C, or further optimizing the fabrication process, or other new strategies. Again, the Si-compatible material and fabrication system is a breakthrough for the integration and practical applications of micro-LIBs with other electronic devices.

3 Postmortem morphologies

The mechanical and morphology properties of the Si–SnO_2 NR composite and Si NRs were investigated after the electrochemical processes. As seen in Fig. 8(a) and the corresponding enlarged image in Fig. 8(e), after 100 cycles at a current density of 100 μA cm^{-2} the Si–SnO_2 NR composite still shows similar morphologies to that in the as-prepared sample exhibiting a good verticality over a large area. However, differently, some wrinkles were produced on the surface of the NR sidewall due to the Si and SnO_2 expansions when Li-ion inserting/de-inserting repeatedly. Also, in a minority of small areas several Si NRs have collapsed and agglomerated to form an umbrella-like cluster as displayed in Fig. 8(b) and (f), which could be ascribed to the unevenness of the local current density during the charge/discharge process. Similar results also can be found in the composite electrode after 200 cycles even at a higher current density of 500 μA cm^{-2} as shown in Fig. S4 (ESI†). In contrast, the post-morphology of the Si NRs after the same electrochemical process displays different phenomena as shown in Fig. 8(c), (g) and (h). Cracks can be seen in the majority of areas of the Si NR arrays as shown in the inset of Fig. 8(c), which is believed to be caused by the un-relaxed stress due to the volume expansion during charge/discharge processes. In the area without cracks as shown in Fig. 8(c), bent and vertical Si NRs randomly take up the whole region as imaged in Fig. 8(g) and (h) respectively. The bent Si NRs can be reasonably ascribed to the damage of the Si NR structure during cycling. According to the above results, it can be evidently deduced that the thin coating layer of the SnO_2 sheath is helpful to alleviate the volume expansion of the Si NR during the Li ion insertion/extraction process. Compared to the 3D Si nanostructures, the post-morphology of the planar Si–SnO_2 after 100 cycles at a lower current density of 20 μA cm^{-2} is also shown in Fig. 8(d) and the corresponding enlarged view of Fig. 8(i). It is obvious that the agglomeration of SnO_2 nanoparticles happens on the exposed Si substrate, which is not seen in Si–SnO_2 NR composites and further proves the advantages of 3D structures with the large surface volume ratio to avoid the aggregation of nanoparticles. As a result, the coating layer of SnO_2 in a 3D distribution would play a more beneficial role on improving the electrochemical properties than a planar morphology. Therefore, the improved cycle performance and CE for the Si–SnO_2 NR composite can be understandably attributed to the following reasons: (i) the bottle-like structure is more mechanically stable on the substrate and thus can reduce the possibilities of collapse and fracture of the Si NRs. (ii) The 3D structure of the samples enlarges the surface area and reduces the current density in contrast to planar Si with the same footprint area, therefore lower the polarization effects. (iii) The Si NRs not only act as structural support but also as the electrode material to enhance the capacity of the battery. (iv) The nanorods or the composites have enough space to release the volume expansion during the lithium ion insertion/extraction into the active materials and thus improve the cycle performance. (v) SnO_2 thin film coverage on the Si NRs can improve the capacity and reduce the volume expansion to a degree: on the one hand, the intermediate product of Sn nanoparticles can improve the surface electronic conductivity and promote kinetics process; on the other hand, the coating layer of the SnO_2 film can prevent the Si NRs directly contacting with the

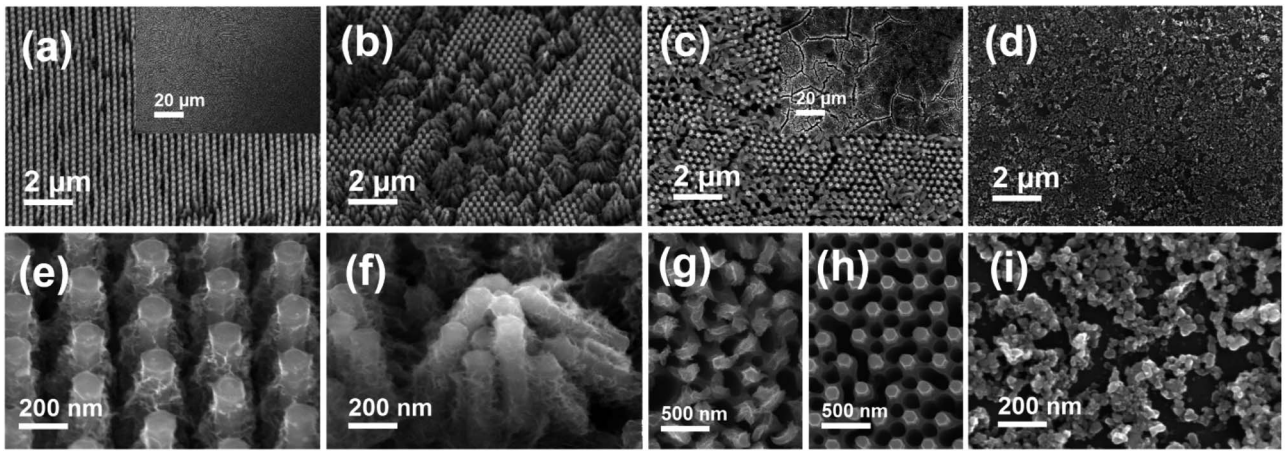

Fig. 8 SEM images of areas (a) and (b) in Si–SnO_2 NR composite electrode and (c) in Si NRs after Li ion insertion/extraction at a current density of 100 μA cm^{-2} within the voltage window between 0.1 and 2.0 V *vs.* Li/Li^+ for 100 cycles; and as a comparison (d) area in planar Si–SnO_2 electrode after 100 cycles at a current density of 20 μA cm^{-2} within the voltage window from 0.13 to 2.0 V *vs.* Li/Li^+; then the corresponding images at higher magnification (e) and (f) from areas of (a) and (b) respectively, (g) and (h) from area of (c), and (i) from area of (d).

electrolyte and would retard the gradual growth of the SEI layer, and therefore enhance the battery life.

Conclusion

In summary, a concept of fabricating 3D hexagonal bottle-like Si NR arrays in wafer scale was realized on Si substrates by using NSL combined dry etching technology. The as-fabricated Si NR arrays with homogeneous morphology and good mechanical structure are anchored to the Si substrate acting as both electrodes and structural reinforcements for the 3D nanoelectrodes in LIBs. An additional sheath of SnO_2 thin film was developed on the outer surface of the Si NRs to improve the capacities and cycle performance by configuring the 3D Si–SnO_2 NR composite electrode arrays. This low cost and large scale process is technically feasible to be introduced to prepare other kinds of Si nanocomposite arrays, such as Si–C, Si–TiO_2 and Si–graphene, in a large area and hexagonal arrangement. Using this Si compatible processing, this kind of 3D core–shell nanostructured electrodes is promising to build reliable and high area capacity microbatteries with the aim of integration with Si-based devices, such as ICs, MEMS/NEMS or other micro/nano electronic devices.

Acknowledgements

This work is financially supported by the National Basic Research Program of China (2009CB930704), National Natural Science Foundation of China (61106118), Natural Science Foundation of Fujian Province of China (2011J01362), and Fundamental Research Funds for the Central Universities (2011121026).

Notes and references

1 H. Sato, C. W. Berry, B. E. Casey, G. Lavella, Y. Yao, J. M. VandenBrooks and M. M. Maharbiz, *IEEE 21st Intl. Conf. Micro Electro Mechanical Systems 2008 (MEMS2008)*, pp. 164–167.
2 M. Perlmutter and L. Robin, *IEEE Position Location and Navigation Symposium (PLANS)*, 2012, pp. 225–229.
3 K. Palem and A. Lingamneni, *IEEE Design Automation Conference (DAC)*, 2012, pp. 924–929.
4 J. M. Tarascon and M. Armand, *Nature*, 2011, **414**, 359–367.
5 K. S. Kang, Y. S. Meng, J. Breger, C. P. Grey and G. Ceder, *Science*, 2006, **311**, 977–980.
6 P. G. Bruce, B. Scrosati and J. M. Tarascon, *Angew. Chem., Int. Ed.*, 2008, **47**, 2930–2946.
7 J. F. M. Oudenhoven, R. J. M. Vullers and R. van Schaijk, *Int. J. Energy Res.*, 2012, **36**, 1139–1150.
8 B. Dunn, J. W. Long and D. R. Rolison, *Electrochem. Soc. Interface*, 2008, 49–53.
9 J. W. Long, B. Dunn, D. R. Rolison and H. S. White, *Chem. Rev.*, 2004, **104**, 4463–4492.
10 T. S. Arthur, D. J. Bates, N. Cirigliano, D. C. Johnson, P. Malati, J. M. Mosby, E. Perre, M. T. Rawls, A. L. Prieto and B. Dunn, *MRS Bull.*, 2011, **36**, 523–531.
11 S. K. Cheah, E. Perre, M. Rooth, M. Fondell, A. Hårsta, L. Nyholm, M. Boman, T. Gustafsson, J. Lu, P. Simon and K. Edstrom, *Nano Lett.*, 2009, **9**, 3230–3233.
12 S. R. Gowda, A. L. M. Reddy, X. Zhan, H. R. Jafry and P. M. Ajayan, *Nano Lett.*, 2012, **12**, 1198–1202.
13 T. Djenizian, I. Hanzu and P. Knauth, *J. Mater. Chem.*, 2011, **21**, 9925–9937.
14 S. R. Gowda, A. L. M. Reddy, M. M. Shaijumon, X. Zhan, L. Ci and P. M. Ajayan, *Nano Lett.*, 2011, **11**, 101–106.
15 M. Kotobuki, Y. Suzuki, H. Munakata, K. Kanamura, Y. Sato, K. Yamamoto and T. Yoshida, *J. Electrochem. Soc.*, 2010, **4**, 493–498.
16 J. F. M. Oudenhoven, L. Baggetto and P. H. L. Notten, *Adv. Energy Mater.*, 2011, **1**, 10–33.
17 L. Baggetto, H. C. M. Knoops, R. A. H. Niessen, W. M. M. Kessels and P. H. L. Notten, *J. Mater. Chem.*, 2010, **20**, 3703–3708.

18 B. A. Boukamp, G. C. Lesh and R. A. Huggins, *J. Electrochem. Soc.*, 1981, **128**, 725–729.
19 U. Kasavajjula, C. S. Wang and A. J. Appleby, *J. Power Sources*, 2007, **163**, 1003–1039.
20 C. K. Chan, R. N. Patel, M. J. O'Connell, B. A. Korgel and Y. Cui, *ACS Nano*, 2010, **4**, 1443–1450.
21 Y. He, B. Yang, K. Yang, C. Brown, R. Ramasamy, H. Wang, C. Lundgren and Y. Zhao, *J. Mater. Chem.*, 2012, **22**, 8294–8303.
22 T. Song, H. Cheng, H. Choi, J.-H. Lee, H. Han, D. H. Lee, D. S. Yoo, M.-S. Kwon, J.-M. Choi, S. G. Doo, H. Chang, J. Xiao, Y. Huang, W. Il Park, Y.-C. Chung, H. Kim, J. A. Rogers and U. Paik, *ACS Nano*, 2012, **6**, 303–309.
23 K. Evanoff, J. Benson, M. Schauer, I. Kovalenko, D. Lashmore, W. Jud Ready and G. Yushin, *ACS Nano*, 2012, **6**, 9837–9845.
24 C. K. Chan, H. Peng, G. Liu, K. McIlwrath, X. F. Zhang, R. A. Huggins and Y. Cui, *Nat. Nanotechnol.*, 2008, **3**, 31–35.
25 C. L. Cheung, R. J. Niolic, C. E. Reinhardt and T. F. Wang, *Nanotechnology*, 2006, **17**, 1339–1343.
26 S. W. Lee, M. T. McDowell, L. A. Berla, W. D. Nix and Y. Cui, *Proc. Natl. Acad. Sci. U. S. A.*, 2012, **109**, 4080–4085.
27 Y. Idota, T. Kubota, A. Matsufuji, Y. Maekawa and T. Miyasaka, *Science*, 1997, **276**, 1395–1397.
28 J. Yin, Y. Zang, C. Yue, Z. Wu, S. Wu, J. Li and Z. Wu, *J. Mater. Chem.*, 2012, **22**, 7902–7909.
29 M. Green, E. Fielder, B. Scrosati, M. Wachtler and J. S. Moreno, *Electrochem. Solid-State Lett.*, 2003, **6**, 75–79.
30 E. L. Memarzadeh, W. Peter Kalisvaart, A. Kohandehghan, B. Zahiri, C. M. B. Holt and D. Mitlin, *J. Mater. Chem.*, 2012, **22**, 6655–6668.
31 S. H. Nam, K. S. Kim, H.-S. Shim, S. H. Lee, G. Y. Jung and W. B. Kim, *Nano Lett.*, 2011, **11**, 3656–3662.
32 X. W. Lou, Y. Wang, C. Yuan, J. Y. Lee and L. A. Archer, *Adv. Mater.*, 2006, **18**, 2325–2329.
33 J. Wang, N. Du, H. Zhang, J. Yu and D. Yang, *J. Phys. Chem. C*, 2011, **115**, 11302–11305.
34 Z. Hong and M. Wei, *J. Mater. Chem. A*, 2013, **1**, 4403–4414.
35 L. Zeng, C. Zheng, L. Xia, Y. Wang and M. Wei, *J. Mater. Chem. A*, 2013, **1**, 4293–4299.
36 L. Zeng, F. Xiao, J. Wang, S. Gao, X. Ding and M. Wei, *J. Mater. Chem.*, 2012, **22**, 14284–14288.
37 L. Zeng, C. Zheng, C. Deng, X. Ding and M. Wei, *ACS Appl. Mater. Interfaces*, 2013, **5**, 2182–2187.
38 M. Roberts, P. Johns, J. Owen, D. Brandell, K. Edstrom, G. El Enany, C. Guery, D. Golodnitsky, M. Lacey, C. Lecoeur, H. Mazor, E. Peled, E. Perre, M. M. Shaijumon, P. Simon and P.-L. Taberna, *J. Mater. Chem.*, 2011, **21**, 9876–9890.
39 W. J. Lee, M.-H. Park, Y. Wang, J. Y. Lee and J. Cho, *Chem. Commun.*, 2010, **46**, 622–624.
40 C.-M. Wang, W. Xu, J. Liu, J.-G. Zhang, L. V. Saraf, B. W. Arey, D. Choi, Z.-G. Yang, J. Xiao, S. Thevuthasan and D. R. Baer, *Nano Lett.*, 2011, **11**, 1874–1880.
41 http://www.catagle.com/1661/ips_thinergy_mec225_product_data_sheet_ds1014_v1–1_final_20110913.htm.